

A Comprehensive Investigation on the Effect of Growth Rate and Composition on Dendritic Microstructure and Arm Spacings in Directionally Solidified Al-Zn Alloys

Emin Çadırılı¹

Hasan Kaya²

Uğur Büyük³

Abstract

Cellular and dendritic microstructures formed during the solidification of alloy systems lead to a non-uniform distribution of solute elements, i.e., microsegregation, significantly influencing the final properties of the material. The scale and morphology of microsegregation are primarily characterized by primary (λ_1) and secondary (λ_2) dendrite arm spacings. This study investigates the directional solidification behavior of three Al-Zn binary alloys with different compositions: Al-7wt.%Zn, Al-10wt.%Zn, and Al-20wt.%Zn. Alloy samples, prepared under vacuum using high-purity (99.99%) starting materials, were unidirectionally solidified in a custom-built Bridgman-type directional solidification furnace under a constant thermal gradient ($G = 10.3$ K/mm) and varying growth rates (V) ranging from $8.25 \mu\text{m/s}$ to $165 \mu\text{m/s}$. From the microstructural images obtained from transverse and longitudinal sections of the solidified samples, the primary (λ_1) and secondary (λ_2) dendrite arm spacings were meticulously measured as a function of zinc concentration (C_0) and growth rate (V). The experimentally determined λ - V

- 1 Prof. Dr., Niğde Ömer Halisdemir University, Faculty of Science, Department of Physics, Niğde, Turkey, ecadirli@gmail.com, ORCID: 0000-0002-8085-9733
- 2 Prof. Dr., Erciyes University, Faculty of Education, Department of Mathematics and Science Education, Kayseri, Turkey, hasankaya@erciyes.edu.tr, ORCID: 0000-0003-3529-9762
- 3 Prof. Dr., Erciyes University, Faculty of Education, Department of Mathematics and Science Education, Kayseri, Turkey, buyuk@erciyes.edu.tr, ORCID: 0000-0002-6830-8349

and λ -Co relationships were mathematically modeled using linear regression analysis, and the obtained findings were comprehensively compared with existing theoretical solidification models and similar experimental studies in the literature. This research provides a fundamental understanding of the microstructural evolution in Al-Zn alloys and offers significant data for the design of desired microstructures, and consequently material properties, through the control of solidification parameters.

INTRODUCTION

Aluminum-Zinc (Al-Zn) alloys, particularly those forming the basis of the high-strength 7000 series, are materials of strategic importance in numerous critical engineering applications, including aerospace, automotive, marine, and defense industries, owing to their low density, superior mechanical performance, good corrosion resistance, and age-hardening capabilities (Polmear, 2006; Davis, 1993). The outstanding properties exhibited by these alloys are largely dependent on the microstructural features developed during the solidification process, especially the dendritic and cellular morphologies, grain size, and the distribution of secondary phases (Porter & Easterling, 1992). Consequently, a thorough understanding of the effects of solidification parameters on microstructural development and the ability to precisely control these relationships are vital requisitos for producing high-performance Al-Zn alloys with desired end-user properties.

Solidification is a fundamental phase transformation wherein a material transitions from a liquid to a solid phase, and the microstructural evolution occurring during this process dictates the macroscopic behavior of the alloy. The solidification of most metals and alloys, particularly in conventional casting methods, often results in a cellular or, more commonly, a dendritic growth morphology due to the destabilization of a planar solid-liquid interface (Kurz & Fisher, 1998). Dendritic structures possess complex, tree-like geometries, comprising primary dendrite trunks and secondary, tertiary, and higher-order arms growing at specific angles from them. This intricate structure leads to a non-uniform distribution of alloying elements and impurities between the dendrite arms and within the dendrite cores, a phenomenon known as microsegregation (Osorio et al., 2006; Flemings, 1974). The extent and scale of microsegregation can significantly affect the material's mechanical strength, ductility, fatigue life, fracture toughness, and corrosion resistance (Ganesan et al., 2021). Therefore, the control of microstructural parameters such as the primary dendrite arm spacing (λ_1) and secondary dendrite arm spacing (λ_2), which are indicative of microsegregation and define the fineness of the dendritic structure, is of

paramount importance. λ_1 refers to the distance between the centers of adjacent dendrites, while λ_2 denotes the average spacing between adjacent secondary arms on the same dendrite. These parameters are primarily dependent on solidification conditions such as the chemical composition of the alloy (Co), the temperature gradient (G) during solidification, and the growth rate (V) (Gündüz & Çadırılı, 2002; Trivedi & Kurz, 1994).

Directional solidification techniques are powerful experimental methods wherein solidification parameters (especially G and V) can be independently controlled, thereby enabling a systematic investigation of microstructural development (Tiller et al., 1953). In directional solidification experiments conducted using Bridgman-type furnaces, the sample is solidified by pulling it at a controlled rate through a fixed temperature gradient. This method is widely employed, particularly for determining the relationship between microstructural scales like λ_1 and λ_2 and the solidification parameters (Burden & Hunt, 1974; Liu et al., 2005). In the literature, theoretical models dependent on solidification parameters have been developed for λ_1 by researchers such as Hunt (1979), Kurz and Fisher (1981), and Trivedi (1984), and for λ_2 by Trivedi and Somboonsuk (1984). These models generally predict that λ_1 is proportional to $V^{-0.25} G^{-0.5}$ and λ_2 is proportional to $V^{-0.5}$ (or similar power-law expressions), although these exponents can vary depending on the alloy system and specific solidification conditions.

Al-Zn alloys also exhibit noteworthy characteristics in terms of their solidification behavior. Aluminum, with its face-centered cubic (FCC) crystal structure, displays a weak anisotropy in its solid-liquid interfacial energy, whereas zinc, having a hexagonal close-packed (HCP) structure, exhibits a pronounced anisotropy (Gonzales & Rappaz, 2006). This difference in anisotropy can influence dendritic growth morphologies and orientations, particularly at high zinc concentrations (Rhême et al., 2008). In the Al-Zn system, the wide solidification range and the equilibrium distribution coefficient (k) of zinc in aluminum being less than unity (Osamura et al., 1985) lead to significant microsegregation. This situation can result in the formation of zinc-rich phases in the interdendritic regions and, consequently, a heterogeneous microstructure.

The primary objective of this study is to experimentally investigate how the primary (λ_1) and secondary (λ_2) dendrite arm spacings change with growth rate (V) and alloy composition (Co) during the directional solidification of Al-Zn binary alloys with different zinc concentrations (Al-7wt.%Zn, Al-10wt.%Zn, and Al-20wt.%Zn). It is aimed to develop a more comprehensive understanding of the solidification behavior of Al-

Zn alloys by comparing the microstructural data obtained from directional solidification experiments conducted under a constant temperature gradient ($G = 10.3 \text{ K/mm}$) over a wide range of growth rates ($8.25\text{-}165 \mu\text{m/s}$) with existing theoretical models and similar experimental studies in the literature. The results obtained are expected to contribute to the optimization of casting and solidification processes for these alloys and, consequently, to the development of materials with superior properties.

MATERIALS AND METHODS

2.1. Alloy Preparation and Directional Solidification Procedure

The Al-xZn ($x = 7, 10, \text{ and } 20 \text{ wt.}\%$) binary alloys investigated in this study were prepared under vacuum using high-purity (99.99%) aluminum and zinc metals. The starting materials, after being precisely weighed according to the desired compositions, were melted in graphite crucibles within an induction furnace under a pressure of approximately 10^{-3} mbar. To ensure complete homogenization of the molten alloy, each composition was held at a temperature approximately 100 K above its melting point for a specific duration (e.g., 30 minutes) and mechanically stirred. Following the homogenization process, each molten alloy was poured into high-density graphite crucibles (4 mm inner diameter, 6.35 mm outer diameter, and 250 mm length) held in a specially designed hot-filling unit. Maintaining the crucibles at a temperature approximately 100 K above the alloy's melting point helped prevent premature solidification during casting and ensured complete filling of the crucible.

Subsequently, each sample was vertically positioned in a custom-built, computer-controlled Bridgman-type directional solidification furnace. The details of the experimental apparatus and procedures have been published in previous studies [14-16]. Unidirectional solidification of the samples was performed under a constant thermal gradient ($G = 10.3 \text{ K/mm}$) established between the heater and cooler zones of the furnace. The maximum operating temperature of the furnace was set to 1250 K. After stabilizing the thermal conditions within the furnace and purging the sample environment with high-purity argon gas, the samples were solidified by pulling them downwards at constant rates ($V = 8.25, 16.5, 41.25, 82.5, \text{ and } 165 \mu\text{m/s}$) by means of five synchronized motors operating at different speeds. After achieving approximately 10-12 cm of steady-state growth, the samples were rapidly quenched by dropping them into a water bath located at the bottom of the furnace to preserve the solid-liquid interface morphology. The temperature of the water in the reservoir was maintained at 283 K with an accuracy of

± 0.1 K using a PolyScience digital 9102 heating/refrigerating circulating bath. The temperature profile and control within the sample were ensured by a Eurotherm 2604 temperature controller operating with an accuracy of ± 0.1 K. All solidification experiments were conducted under the specified constant temperature gradient ($G = 10.3$ K/mm) and varying growth rates ($V = 8.25$ - 165 $\mu\text{m/s}$).

2.2. Measurement of Solidification Parameters (G, V) and Metallographic Preparation

The temperature within the specimen was measured by three K-type (Chromel-Alumel) insulated thermocouples, 0.50 mm in diameter, fixed axially within the sample at intervals of 10-20 mm. The ends of the thermocouples were connected to a measurement unit consisting of a data-logger and a computer. Cooling rates and temperature data were continuously recorded via the computer during growth. When the solid-liquid interface was at the level of the second thermocouple, the temperature difference (ΔT) between the first and second thermocouples was read from the data-logger record. The time taken (Δt) for the solid-liquid interface to pass between the thermocouples separated by known distances was also obtained from the data-logger record. Thus, the growth rate ($V = \Delta X / \Delta t$, where ΔX is the known distance between thermocouples) for each sample and the temperature gradient ($G = \Delta T / \Delta X$) in the liquid phase were determined using the measured values of Δt , ΔT , and the known value of ΔX .

After quenching, the samples were removed from the graphite crucibles, and sections of approximately 3 cm in length from the top and bottom, which did not represent the steady-state growth region, were cropped off and discarded. Longitudinal (parallel to the solidification direction) and transverse (perpendicular to the solidification direction) sections of the remaining samples were taken and cold-mounted in epoxy resin for standard metallographic procedures. The mounted sample surfaces were first progressively ground under water using silicon carbide (SiC) abrasive papers of increasing fineness (e.g., 220, 400, 600, 800, 1200, and 2500 grit). Subsequently, they were mechanically polished on polishing cloths using diamond paste of 6 μm , 3 μm , 1 μm , and 1/4 μm successively, with appropriate lubricants. To reveal the microstructure, the polished sample surfaces were etched for approximately 35 seconds with Keller's reagent (1.5% HCl – 0.5% HF – 2.5% HNO₃ – 95.5% H₂O, by volume). Following metallographic preparation, the microstructures of the samples were examined from both transverse and longitudinal sections using a Nikon Eclipse MA100 optical microscope, and digital images were captured.

2.3. Measurement of Microstructural Parameters (λ_1 and λ_2)

The primary dendrite arm spacing (λ_1), as schematically shown in Fig. 1, was determined by measuring the distance between the centers of two adjacent dendrites in the transverse sections. Two different methods were used to measure the λ_1 values:

1. **Triangle Method:** In this method, a triangle is formed by joining the centers of three neighboring dendrites, and the side lengths of this triangle are recorded as $\lambda_1(\text{tr})$.
2. **Area Counting Method:** In this method, the average primary dendrite arm spacings, $\lambda_1(\text{ar})$, were determined from the microstructural images of the sample's cross-section (Fig. 1) using the following equation:

$$\lambda_1(\text{ar}) = (A / (M^2N))^{0.5}$$

where M is the microscope magnification factor, A is the total cross-sectional area on the image, and N is the number of primary dendrites within that area.

The average primary dendrite arm spacing ($\lambda_1(\text{ave})$) reported for each sample was calculated by taking the arithmetic mean of numerous $\lambda_1(\text{tr})$ and $\lambda_1(\text{ar})$ measurements obtained from different regions. At least 50-100 λ_1 measurements were made from different regions for each sample.

The secondary dendrite arm spacing (λ_2) was measured by averaging the distances between adjacent secondary arms on the longitudinal section of a primary dendrite. Each reported λ_2 value represents the average of numerous (typically 5-10 per primary dendrite) secondary arm spacing measurements taken from at least 20-30 different primary dendrites for each specimen. All microstructural measurements were performed on calibrated microscope images using image analysis software.

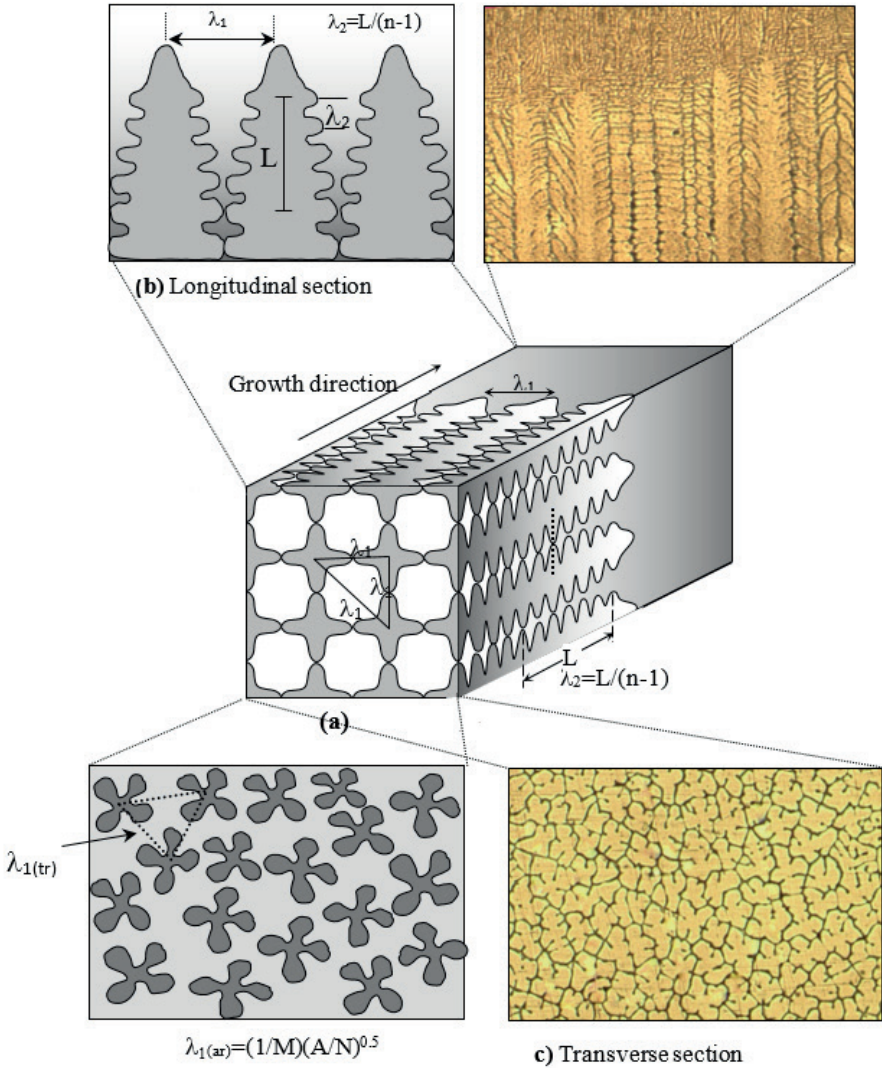


Fig. 1. (a) Schematic illustration of the dendritic spacings measurements longitudinal and transverse sections (b) longitudinal section (c) transverse section (M : magnification factor, A : total area)

3. RESULTS AND DISCUSSION

3.1. Microstructural Characterization and Phase Analysis

Energy Dispersive X-ray Spectroscopy (EDX) analyses were performed on quenched samples to determine the phases formed and the solute distribution at the solid-liquid interface in Al-Zn alloys. The analyses were

conducted at an accelerating voltage of 20 keV using X-ray lines. The EDX spectra and point analysis results, shown in Fig. 2, illustrate the solute (Zn) concentrations in the solid and liquid phases at selected regions of the solid-liquid (S/L) interface.

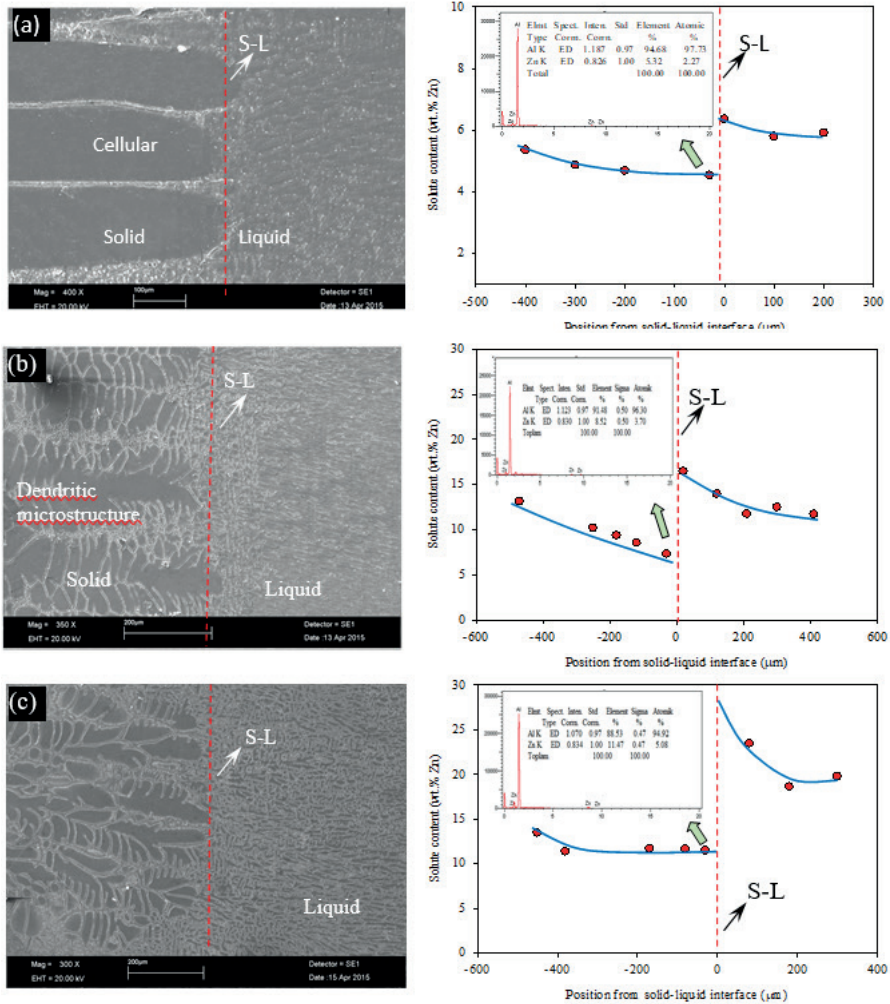


Fig. 2 The solute concentrations of the solid and liquid phases at the S/L interface and EDX spectrums for Al-Zn alloys; (a) Al-7wt.% Zn (b) Al-10wt.% Zn (c) Al-20wt.% Zn

For the different Al-Zn alloy compositions (Al-7wt.%Zn, Al-10wt.%Zn, and Al-20wt.%Zn), zinc (Zn) concentrations were measured in both solid and liquid phases. The Zn concentrations in the solid phase (dendrite core) regions were observed to be approximately constant and lower than

the nominal composition values of the alloy. This can be attributed to the equilibrium distribution coefficient (k) of the Al-Zn system being less than unity ($k < 1$). Solidification commences with the formation of a solid phase containing less Zn than the nominal composition, which causes the dendrite core to have a higher melting temperature compared to the surrounding liquid (Chen et al., 2013). As clearly depicted in Fig. 2, as solidification progresses, solute Zn atoms are rejected from the solidifying interface into the liquid phase, leading to a solute pile-up ahead of the S/L interface. This accumulation causes the Zn concentration in the liquid phase at the interface to exceed the nominal value. Moving away from the S/L interface into the bulk liquid, the Zn concentration gradually decreases, eventually approaching the nominal compositions of the alloy (Al-7wt.%Zn, Al-10wt.%Zn, and Al-20wt.%Zn). This solute distribution profile reflects a typical dendritic solidification behavior.

3.2. Effect of Solidification Parameters on Microstructural Morphology

The experimental results clearly demonstrate that solidification parameters (growth rate V and alloy composition C_0) have a strong influence on the solidification morphology of Al-Zn alloys. Under a constant temperature gradient ($G = 10.3$ K/mm), cellular and dendritic microstructures were obtained at growth rates ranging from $8.25 \mu\text{m/s}$ to $165 \mu\text{m/s}$. Figures 3 and 4 present typical optical micrographs showing the transition from cellular to dendritic microstructure in the longitudinal and transverse sections of Al-Zn alloys with increasing V and C_0 .

At low growth rates (e.g., around $V < 16.5 \mu\text{m/s}$), a cellular morphology was generally observed, whereas with increasing growth rate, the stability of the solid-liquid interface decreased, leading to a transition to dendritic growth. The cellular-to-dendritic transition was found to be completed at a growth rate of approximately $16.5 \mu\text{m/s}$ for all Al-Zn alloy compositions. As the growth rate (V) and zinc concentration (C_0) increased, the dendritic structure became more pronounced, and the dendrite arm spacings (both λ_1 and λ_2) tended to decrease. This indicates the formation of a finer microstructure at higher growth rates and higher alloy concentrations. The Cellular to Dendritic Transition (CDT) has been investigated by several researchers in the literature (Tewari & Laxmanan, 1987; Georgelin & Pocheau, 1998; Wei et al., 2015). However, a definitive criterion for CDT has not yet been fully established, and it is known that this transition depends on several factors, including the G/V ratio and alloy parameters.

The morphological changes observed in this study are in general agreement with the trends reported in the literature.

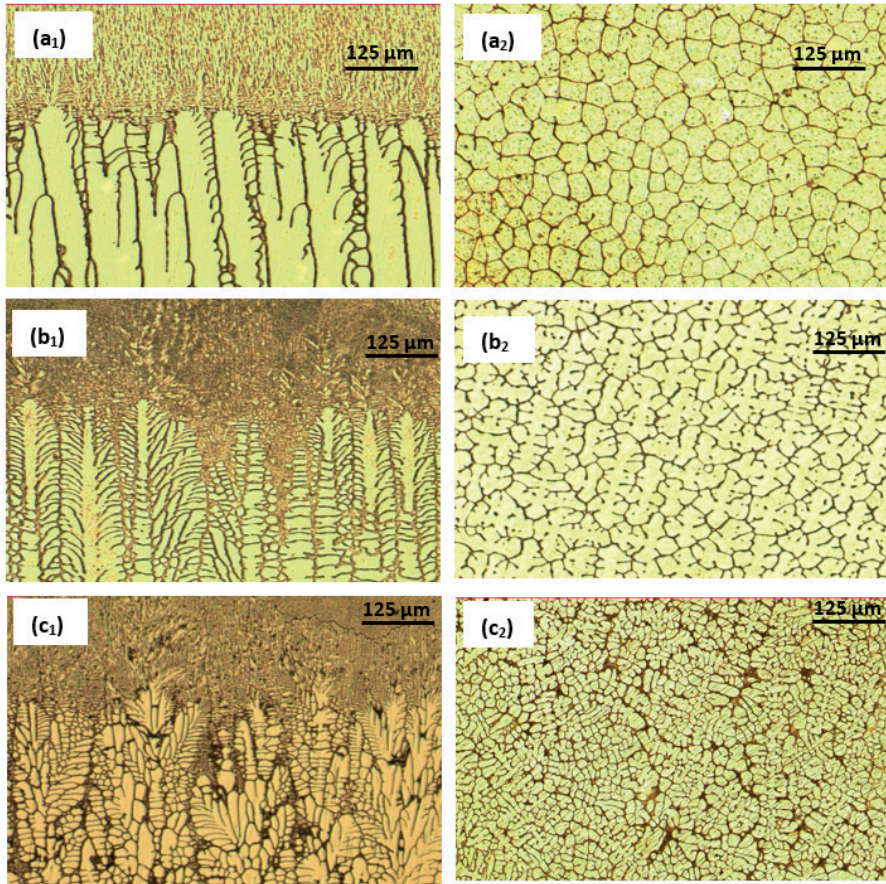


Fig. 3. Optical micrographs of Al-Zn alloys under $V=41.25$ m/s and $G=10.3$ K/mm solidification condition (a_p, a_2) Al-5 wt.% Zn, (b_p, b_2) Al-10 wt.% Zn, (c_p, c_2) Al-20 wt.% Zn

3.3. Effect of Growth Rate and Composition on Microstructural Parameters (λ_1 and λ_2)

3.3.1. Effect of Growth Rate (V)

Experimental results show that under a constant temperature gradient ($G = 10.3$ K/mm), both primary (λ_1) and secondary (λ_2) dendrite arm spacings decrease with increasing growth rate (V) for all alloy compositions (Figs. 4a and 4b). This behavior is consistent with solidification theories;

higher growth rates lead to shorter diffusion distances at the solid-liquid interface and faster heat extraction, thereby promoting the formation of a finer dendritic structure.

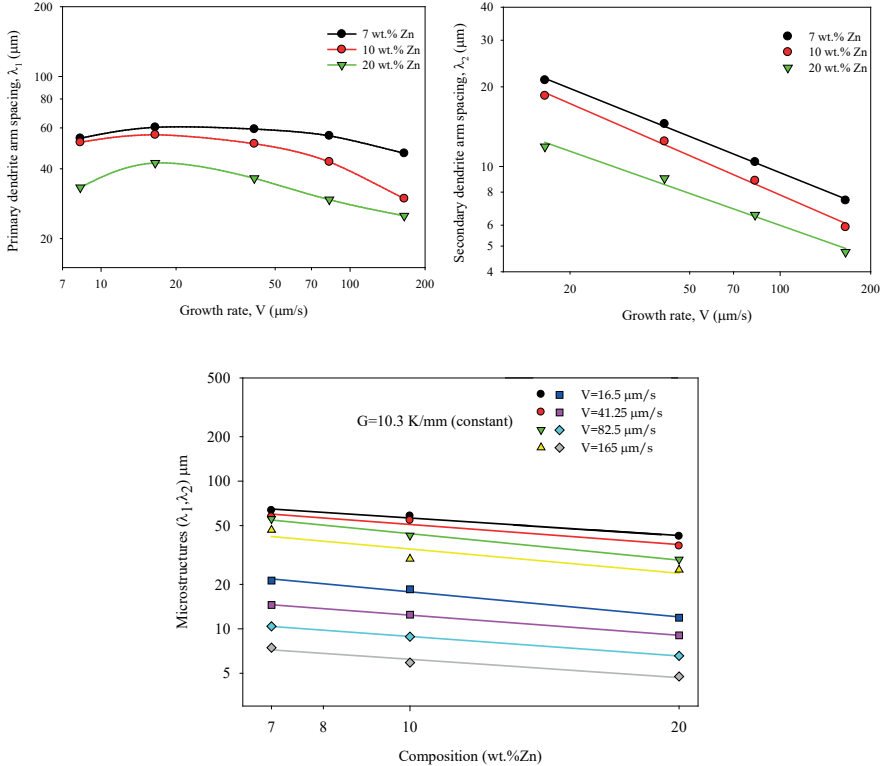


Fig. 4 (a) Variation of the primary dendritic arm spacing with the growth rate, (b) Variation of the secondary dendritic arm spacing with the growth rate.

Based on the experimental data obtained, the relationship between the microstructural parameters (λ_1 and λ_2) and the growth rate (V) can be expressed by a power law of the following general form:

$$\lambda_1 = k_1 (V^{-a})$$

$$\lambda_2 = k_2 (V^{-b})$$

Here, k_1 and k_2 are proportionality constants, and a and b represent the exponent values of the growth rate for λ_1 and λ_2 , respectively. Table I presents these relationships obtained for different Al-Zn compositions, along with the constants (k) and correlation coefficients (r).

Table 1. The relationships among the dendritic spacings (λ_1, λ_2) growth velocity (V) and composition (Co)

Composition (wt.%)	Relationships	Constant (k)	Correlation coefficient (r)
Al-7 Zn	$\lambda_1 = k_1 V^{0.27}$ $\lambda_2 = k_2 V^{0.45}$	$k_1 = 209 \mu\text{m}^{1.27} \text{s}^{-0.27}$ $k_2 = 89 \mu\text{m}^{1.45} \text{s}^{-0.45}$	$r_1 = -0.987$ $r_2 = -0.998$
Al-10 Zn	$\lambda_1 = k_3 V^{0.26}$ $\lambda_2 = k_4 V^{0.49}$	$k_3 = 190 \mu\text{m}^{1.26} \text{s}^{-0.26}$ $k_4 = 76 \mu\text{m}^{1.49} \text{s}^{-0.49}$	$r_3 = -0.927$ $r_4 = -0.995$
Al-20 Zn	$\lambda_1 = k_5 V^{0.23}$ $\lambda_2 = k_6 V^{0.40}$	$k_5 = 115 \mu\text{m}^{1.23} \text{s}^{-0.23}$ $k_6 = 37 \mu\text{m}^{1.40} \text{s}^{-0.40}$	$r_5 = -0.975$ $r_6 = -0.998$
Growth rate ($\mu\text{m/s}$)	Relationships	Constant(k)	Correlation coefficient (r)
16.5	$\lambda_1 = k_7 C_o^{-0.32}$ $\lambda_2 = k_8 C_o^{-0.53}$	$k_7 = 178 \mu\text{m}$ (wt.%) ^{0.32}	$r_7 = -0.960$ $r_8 = -0.992$
41.3	$\lambda_1 = k_9 C_o^{-0.38}$ $\lambda_2 = k_{10} C_o^{-0.45}$	$k_8 = 59 \mu\text{m}$ (wt.%) ^{0.53}	$r_9 = -0.890$ $r_{10} = -0.999$
82.5	$\lambda_1 = k_{11} C_o^{-0.32}$ $\lambda_2 = k_{12} C_o^{-0.44}$	$k_9 = 155 \mu\text{m}$ (wt.%) ^{0.38}	$r_{11} = -0.893$ $r_{12} = -0.999$
165.0	$\lambda_1 = k_{13} C_o^{-0.27}$ $\lambda_2 = k_{14} C_o^{-0.43}$	$k_{10} = 35 \mu\text{m}$ (wt.%) ^{0.45} $k_{11} = 115 \mu\text{m}$ (wt.%) ^{0.32} $k_{12} = 25 \mu\text{m}$ (wt.%) ^{0.44} $k_{13} = 81 \mu\text{m}$ (wt.%) ^{0.27} $k_{14} = 17 \mu\text{m}$ (wt.%) ^{0.43}	$r_{13} = -0.965$ $r_{14} = -0.986$

λ_1 : the values of the primary dendrite arm spacing measured from the transverse section

λ_2 : the values of the secondary dendrite arm spacing measured from the longitudinal section of the samples

The exponent values of V for the primary dendrite arm spacing (λ_1), denoted as 'a', as detailed in Table 1, were found to be 0.27, 0.26, and 0.23 for Al-7wt.%Zn, Al-10wt.%Zn, and Al-20wt.%Zn alloys, respectively. These values are in close agreement with the exponent values obtained by Fan et al. (2011) (0.30), Lapin et al. (2011) (0.24, 0.25), and Kaya et al. (2009, 2007) (0.24, 0.28) for Al-based alloys under similar solidification conditions. Furthermore, the exponent values obtained in this study (0.27, 0.26, and 0.23) are also very close to the theoretical exponent value of 0.25 predicted for λ_1 by the models of Hunt (1979), Kurz-Fisher (1981), and Trivedi (1984). In contrast, the exponent values of 0.37 and 0.69 reported by Wang et al. (2010) and Feng et al. (1999), respectively, are significantly higher than those obtained in this work; these differences are likely due to

variations in the alloy system, solidification conditions, and measurement techniques. The exponent values of V for the secondary dendrite arm spacing (λ_2), denoted as 'b', also presented in Table 1, were determined to be 0.45, 0.49, and 0.40 for Al-7wt.%Zn, Al-10wt.%Zn, and Al-20wt.%Zn alloys, respectively. These exponent values are in good agreement with the values of 0.54 and 0.48 found by Wang et al. (2010) and Kaya et al. (2009, 2007) for Al-based alloys. Moreover, the growth rate exponents obtained in this study (0.45, 0.49, and 0.40) are also very close to the theoretical exponent value of 0.50 predicted for λ_2 by the Trivedi-Somboonsuk (1984) model.

3.3.2. Effect of Alloy Composition (Co)

Figure 4c illustrates the variation of λ_1 and λ_2 as a function of Zn concentration (Co) at different growth rates. It was observed that both λ_1 and λ_2 values decrease with increasing Zn composition. For instance, at the lowest growth rate (16.5 $\mu\text{m/s}$), the λ_1 value decreases from approximately 60.39 μm for Al-7wt.%Zn to approximately 42.37 μm for Al-20wt.%Zn. Similarly, the λ_2 values decrease from approximately 21.21 μm for Al-7wt.%Zn to approximately 11.89 μm for Al-20wt.%Zn at the lowest growth rate (16.5 $\mu\text{m/s}$). This behavior can be attributed to the fact that an increasing concentration of alloying element widens the solidification range and influences solute redistribution, leading to the formation of a finer microstructure. The relationship between the microstructural parameters (λ_1 and λ_2) and the alloy composition (Co) can also be expressed by a similar power law:

$$\lambda_1 = k_3 (\text{Co}^{-c})$$

$$\lambda_2 = k_4 (\text{Co}^{-d})$$

Table 1 provides the exponent values (c and d) and constants showing the effect of Co on λ_1 and λ_2 for different growth rates. As seen from Table 1, the exponent values of Co for λ_1 , denoted as 'c', were found to be 0.32, 0.38, 0.32, and 0.27 for growth rates of 16.5, 41.3, 82.5, and 165 $\mu\text{m/s}$, respectively. Similarly, for λ_2 , the exponent values of Co, denoted as 'd', reported in Table 1 are 0.53, 0.45, 0.44, and 0.43 for the same respective growth rates. These exponent values show general agreement with similar studies in literature, although specific values may vary depending on the solidification conditions and alloy system.

3.4. Comparison of Experimental Results with Theoretical Models

3.4.1. Primary Dendrite Arm Spacing (λ_1)

The experimentally obtained λ_1 values in this study were compared with the λ_1 values calculated using the theoretical models proposed by Hunt (1979), Kurz-Fisher (1981), and Trivedi (1984). These comparisons are presented in Figs. 5 (a-c) for different Al-Zn alloy compositions. The physical parameters of Al-Zn alloys used in the theoretical calculations are given in the Appendix. As can be seen from Fig. 5, the λ_1 values calculated with the Hunt model show a very good agreement with the experimentally obtained λ_1 values. This indicates that the Hunt model can successfully predict the primary dendrite arm spacing of Al-Zn alloys under the present experimental conditions. On the other hand, the λ_1 values calculated with the Trivedi and Kurz-Fisher models were generally slightly higher than the experimental values. These discrepancies may arise from the assumptions underlying the models, the accuracy of the material parameters used, and potential deviations in the experimental conditions. In particular, the selection of the L parameter (harmonic perturbation constant) in the Trivedi model can influence the results.

3.4.2. Secondary Dendrite Arm Spacing (λ_2)

The experimentally obtained λ_2 values in this study as a function of growth rate were compared with the λ_2 values calculated using the Trivedi-Somboonsuk (1984) model. This comparison is presented in Fig. 6. As shown in Fig. 6, the λ_2 values calculated from the Trivedi-Somboonsuk model as a function of $(Co V)^{-0.5}$ exhibit very good agreement with our experimental data. This demonstrates that the Trivedi-Somboonsuk model can successfully predict the secondary dendrite arm spacing for the investigated Al-Zn alloys and solidification conditions.

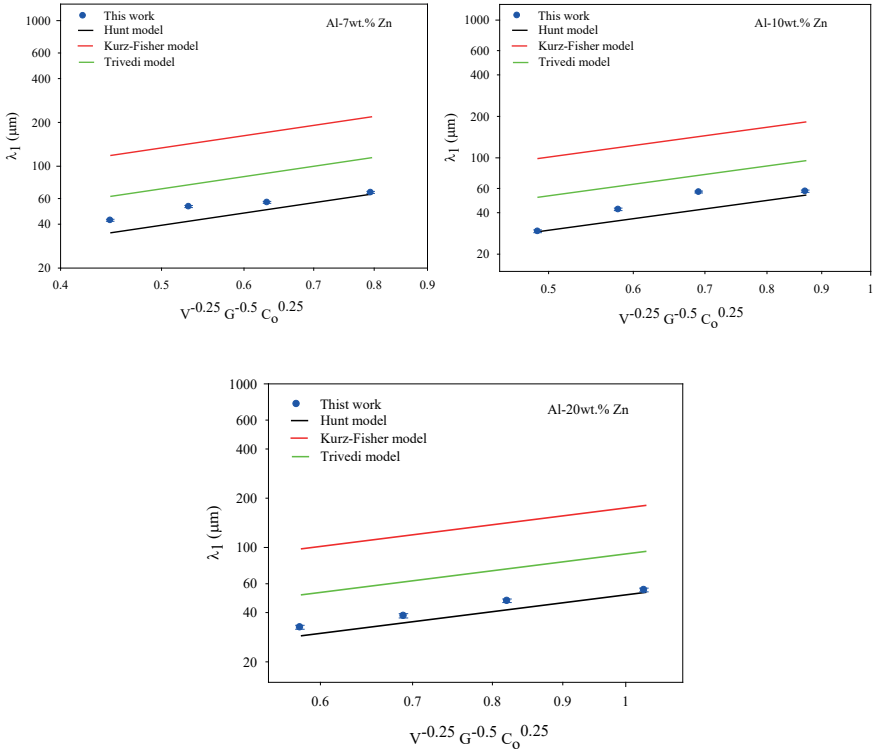


Fig. 5. Comparison of the primary dendrite arm spacings, λ_1 obtained in this work with the theoretical models for (a) Al-wt.7 % Zn alloys, (b) Al-wt.10 % Zn alloys, (c) Al-wt.20 % Zn alloys

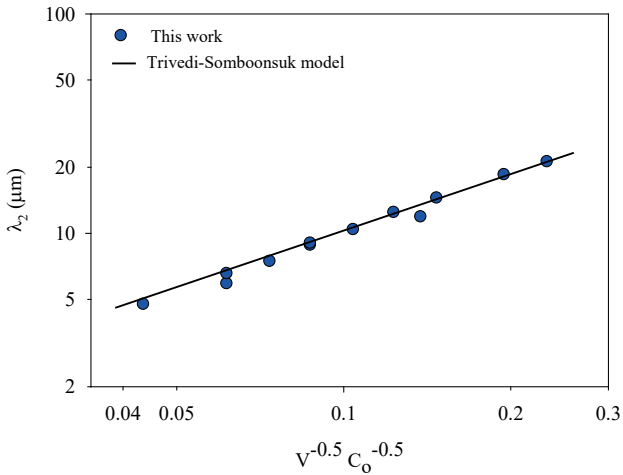


Fig. 6. Comparison of the secondary dendrite arm spacings, obtained in this work with the Trivedi-Somboonsuk model.

4. DISCUSSION AND CONCLUSION

In this study, three Al-Zn binary alloys with different compositions, Al-7wt.%Zn, Al-10wt.%Zn, and Al-20wt.%Zn, were unidirectionally solidified under a constant temperature gradient ($G = 10.3 \text{ K/mm}$) and over a wide range of growth rates ($V = 8.25\text{--}165 \text{ }\mu\text{m/s}$). The microstructural features of the solidified samples were analyzed, and the influence of solidification parameters (V and C_0) on the primary (λ_1) and secondary (λ_2) dendrite arm spacings was investigated. The principal findings and their place in the literature can be discussed as follows:

The variation of solidification morphology with growth rate and composition is one of the significant findings of this study. A cellular microstructure was observed at low growth rates ($<16.5 \text{ }\mu\text{m/s}$), while a transition from cellular to dendritic occurred at approximately $16.5 \text{ }\mu\text{m/s}$ as the growth rate increased. This transition rate is a consequence of the stability of the solid-liquid interface, which can be explained by the Mullins-Sekerka instability theory (Mullins & Sekerka, 1964) and constitutional supercooling criteria (Tiller et al., 1953). As the growth rate increases, solute pile-up ahead of the interface intensifies, leading to higher constitutional supercooling and thus destabilization of the interface, transforming it into a dendritic structure. Regular dendritic structures were formed at growth rates between $16.5 \text{ }\mu\text{m/s}$ and $165 \text{ }\mu\text{m/s}$, with the finest dendrites obtained at the highest growth rate ($165 \text{ }\mu\text{m/s}$). These observations are in general agreement with similar directional solidification studies on Al-based alloys in the literature (Gündüz & Çadırılı, 2002; Tewari & Laxmanan, 1987).

It was determined that both primary (λ_1) and secondary (λ_2) dendrite arm spacings decreased with increasing growth rate (V). This decrease was successfully described by power laws of the form $\lambda_1 \propto V^{-a}$ and $\lambda_2 \propto V^{-b}$ (where a and b are the exponents). The 'a' exponent value obtained for λ_1 (0.27, 0.26, and 0.23 for different Zn compositions) show excellent agreement with the theoretical models proposed by Hunt (1979), Kurz-Fisher (1981), and Trivedi (1984), which predict a $\lambda_1 \propto V^{-0.25}$ relationship. Similarly, the 'b' exponent values obtained for λ_2 (0.45, 0.49, and 0.40 for different Zn compositions) exhibit very good consistency with the theoretical model proposed by Trivedi-Somboonsuk (1984), which predicts a $\lambda_2 \propto V^{-0.5}$ relationship. This agreement confirms the capability of these theoretical models to accurately predict dendrite arm spacings for the investigated Al-Zn alloy system and experimental conditions. The proximity of the experimental exponents to the theoretical values suggests that the

directional solidification process was largely diffusion-controlled and that other effects, such as convection, were minimized.

Regarding the effect of alloy composition (Co), it was observed that both λ_1 and λ_2 values decreased with increasing zinc concentration. This behavior was expressed by power laws of the form $\lambda_1 \propto Co^{-c}$ and $\lambda_2 \propto Co^{-d}$ (where c and d are the exponents). The 'c' exponent values obtained for λ_1 (in the range of 0.27-0.38 for different growth rates) are in good agreement with the $Co^{0.25}$ term present in the models of Hunt (1979), Kurz-Fisher (1981), and Trivedi (1984). The 'd' exponent values obtained for λ_2 (in the range of 0.44-0.53 for different growth rates) show a noteworthy similarity with the $Co^{0.5}$ dependency that can be derived from the Trivedi-Somboonsuk (1984) model (as the ΔT_0 term in the model is dependent on Co). These results indicate that an increasing amount of alloying element promotes the formation of finer microstructures by increasing the solidification range and affecting solute redistribution. A decrease in dendrite arm spacings generally leads to improvements in the mechanical properties of the material, particularly in strength and ductility (Kirkwood, 1984), as finer dendrites imply a more homogeneous solute distribution and smaller segregation distances.

The excellent agreement of the experimental λ_1 values with the Hunt (1979) model reveals that this model is quite successful in predicting the primary dendrite arm spacing of Al-Zn alloys under the present experimental conditions. The slightly higher results from the Trivedi (1984) and Kurz-Fisher (1981) models compared to the experimental values may stem from some of the assumptions inherent in these models or from deviations in the material parameters used from the actual situation. Similarly, the excellent agreement shown by the experimental λ_2 values with the Trivedi-Somboonsuk (1984) model confirms that this model is a reliable tool for predicting secondary dendrite arm spacing in Al-Zn alloys.

This study also has some limitations. For example, only a single temperature gradient value was used. Investigating the effect of different temperature gradients on microstructural evolution could provide a more comprehensive picture of the solidification behavior. Furthermore, this study focused on binary Al-Zn alloys; the solidification behavior of multicomponent Al-Zn alloys, which are frequently used in industrial applications, can be more complex and may constitute an area for future studies.

In conclusion, the principal findings obtained in this study can be summarized as follows:

1. In Al-(7, 10, 20)wt.%Zn alloys, a cellular microstructure was formed at low growth rates ($<16.5 \mu\text{m/s}$), while a transition from cellular to dendritic was observed at growth rates above approximately $16.5 \mu\text{m/s}$. Regular dendritic structures were formed at growth rates between $16.5 \mu\text{m/s}$ and $165 \mu\text{m/s}$, with finer dendrites obtained at increasing growth rates.
2. Primary (λ_1) and secondary (λ_2) dendrite arm spacings decreased with increasing growth rate (V). The exponent values of V for λ_1 ($a \approx 0.23-0.27$) and for λ_2 ($b \approx 0.40-0.49$) showed very good agreement with the theoretical models ($V^{-0.25}$ and $V^{-0.5}$) proposed by Hunt, Kurz-Fisher, Trivedi, and Trivedi-Somboonsuk, respectively.
3. Primary (λ_1) and secondary (λ_2) dendrite arm spacings decreased with increasing zinc concentration (C_0). The exponent values of C_0 for λ_1 ($c \approx 0.27-0.38$) and for λ_2 ($d \approx 0.43-0.53$) exhibited good agreement with the values predicted by the relevant theoretical models ($C_0^{-0.25}$ and $C_0^{-0.5}$).
4. Experimental λ_1 values showed excellent agreement with the Hunt model, and λ_2 values showed excellent agreement with the Trivedi-Somboonsuk model. This confirms that these models can successfully predict dendrite arm spacings for the investigated Al-Zn alloy system and solidification conditions.

These results provide important insights into the directional solidification behavior of Al-Zn alloys and can contribute to the optimization of casting and solidification processes for these alloys, thereby enabling the achievement of desired microstructural features and, consequently, superior material performance.

References

- Burden, M. H., & Hunt, J. D. (1974). Macroscopic stability of a planar, cellular or dendritic interface during directional freezing. *Journal of Crystal Growth*, 20(2), 121–124.
- Chen, Z., Mo, Y., & Nie, Z. (2013). Effect of Zn content on the microstructure and properties of super-high strength Al-Zn-Mg-Cu alloys. *Metallurgical and Materials Transactions A*, 44(8), 3910–3920.
- Davis, J. R. (Ed.). (1993). *Aluminum and aluminum alloys*. ASM International.
- Du, Y., Chang, Y., Huang, B., Gong, W., Jin, Z., Xu, H., Yuan, Z., Liu, Y., He, Y., & Xie, F. Y. (2003). Diffusion coefficients of some solutes in FCC and liquid Al: Critical evaluation and correlation. *Materials Science and Engineering A*, 363(1-2), 140–151.
- Fan, J., Li, X., Su, Y., Chen, R., Guo, J., & Fu, H. (2011). Directional solidification of Ti-49 at.%Al alloy. *Applied Physics A*, 105(1), 239–248.
- Feng, J., Huang, W. D., Lin, X., Pan, Q. Y., Li, T., & Zhou, Y. H. (1999). Primary cellular/dendritic spacing selection of Al-Zn alloy during unidirectional solidification. *Journal of Crystal Growth*, 197(1-2), 393–395.
- Flemings, M. C. (1974). *Solidification processing*. McGraw-Hill.
- Ganesan, A., Garg, R., & Ratke, L. (2021). Microsegregation in metallic alloys: A review on experimental and numerical studies. *Progress in Materials Science*, 121, 100830.
- Georgelin, M., & Pocheau, A. (1998). Onset of sidebranching in directional solidification. *Physical Review E*, 57(3), 3189–3203.
- Gonzales, F., & Rappaz, M. (2006). Dendrite growth directions in aluminum-zinc alloys. *Metallurgical and Materials Transactions A*, 37(9), 2797–2806.
- Gündüz, M., & Çadırılı, E. (2002). Directional solidification of aluminium-copper alloys. *Materials Science and Engineering: A*, 327(1-2), 167–185.
- Hansen, M. (Ed.). (1958). *Constitution of binary alloys*. McGraw-Hill.
- Hunt, J. D. (1979). Solidification and casting of metals. *The Metal Society, London*, 3-9s.
- Jones, H. (1982). *Rapid solidification of metals and alloys*. The Institution of Metallurgists Northway House.
- Kaya, H., Çadırılı, E., & Gündüz, M. (2007). Dendritic growth in an aluminum-silicon alloy. *Journal of Materials Engineering and Performance*, 16(1), 12–21.
- Kaya, H., Çadırılı, E., & Gündüz, M. (2009). Directional cellular growth of Al-2wt%Li bulk samples. *Applied Physics A*, 94(1), 155–165.
- Kirkwood, D. H. (1984). Microsegregation. *Materials Science and Engineering*, 65(1), 101–109.

- Kurz, W., & Fisher, D. J. (1981). Dendritic growth and limit of stability tip radius and spacing. *Acta Metallurgica*, 29(1), 11–20.
- Kurz, W., & Fisher, D. J. (1998). *Fundamentals of solidification* (4th ed.). Trans Tech Publications.
- Lapin, J., & Gabalcová, Z. (2011). Solidification behaviour of TiAl-based alloys studied by directional solidification technique. *Intermetallics*, 19(6), 797–804.
- Liu, Y. C., Han, Y., Yang, G. C., & Zhou, Y. H. (2005). Primary cellular/dendritic spacing selection in rapidly solidified peritectic alloy. *Materials Letters*, 59(23), 2915–2919.
- Morris, J. R., Mendeleev, M. I., & Srolovitz, D. J. (2007). A comparison of crystal-melt interfacial free energies using different Al potentials. *Journal of Non-Crystalline Solids*, 353(37-39), 3565–3569.
- Mullins, W. W., & Sekerka, R. F. (1964). Stability of a planar interface during solidification of a dilute binary alloy. *Journal of Applied Physics*, 35(2), 444–451.
- Osamura, K., Okuda, H., & Ochiai, S. (1985). Isothermal phase decomposition diagram in Al-Zn binary alloys. *Scripta Metallurgica*, 19(12), 1379–1384.
- Osorio, W. R., Spinelli, J. E., Cheung, N., & Garcia, A. (2006). Secondary dendrite arm spacing and solute redistribution effects on the corrosion resistance of Al–10 wt% Sn and Al–20 wt% Zn alloys. *Materials Science and Engineering: A*, 420(1-2), 179–186.
- Polmear, I. J. (2006). *Light alloys: From traditional alloys to nanocrystals* (4th ed.). Butterworth-Heinemann.
- Porter, D. A., & Easterling, K. E. (1992). *Phase transformations in metals and alloys* (2nd ed.). Chapman & Hall.
- Rhême, M., Gonzales, F., & Rappaz, M. (2008). Growth directions in directionally solidified Al-Zn and Zn-Al alloys near eutectic composition. *Scripta Materialia*, 59(4), 440–443.
- Rosa, D. M., Spinelli, J. E., & Garcia, A. (2006). Tertiary dendrite arm spacing during downward transient solidification of Al-Cu and Al-Si alloys. *Materials Letters*, 60(15), 1871–1874.
- Shibuta, Y., Sakane, S., & Suzuki, T. (2017). Anisotropy of solid-liquid interfacial free energy for hexagonal close-packed metals: A molecular dynamics study. *Journal of Chemical Physics*, 146(9), 094702.
- Tewari, S. N., & Laxmanan, V. (1987). Cellular-dendritic transition in directionally solidified binary alloys. *Metallurgical Transactions A*, 18(1), 167–170.

- Tiller, W. A., Jackson, K. A., Rutter, J. W., & Chalmers, B. (1953). The redistribution of solute atoms during the solidification of metals. *Acta Metallurgica*, 1(4), 428-437.
- Trivedi, R. (1984). Interdendritic spacing: Part II. A. Comparison of theory and experiment. *Metallurgical Transactions A*, 15(6), 977-982.
- Trivedi, R., & Kurz, W. (1994). Dendritic growth. *International Materials Reviews*, 39(2), 49-74.
- Trivedi, R., & Somboonsuk, K. (1984). Constrained dendritic growth and spacing. *Materials Science and Engineering*, 65(1), 65-74.
- Wang, K., Lu, S., Mi, G., Li, C., & Fu, H. (2010). Simulation of microstructural evolution in directional solidification of Ti-45at.%Al alloy using cellular automaton method. *China Foundry*, 7(1), 47-51.
- Wei, L., Lin, X., Wang, M., & Huang, W. D. (2015). Effects of physical parameters on the cell-to-dendrite transition in directional solidification. *Chinese Physics B*, 24(7), 078108.

Appendix: Some physical properties of Al-Zn alloys

Property	Symbol	Unit	Value	Ref.
Melting point	T_m	K	933	Du et al. (2003)
Slope of liquid line (Zn in Al)	m_L	K (% wt) ⁻¹	-2.93	Hansen (1958)
Diffusion coefficient (liq., Zn in Al)	D_L	$\mu\text{m}^2\text{s}^{-1}$	1200	Du et al. (2003)
Distribution coefficient (Zn in Al)	k		0.45	Du et al. (2003)
Gibbs-Thomson coefficient	Γ	$\mu\text{m.K}$	0.105	Morris et al. (2007)
The harmonic perturbations (L for Trivedi model)	L	mJ/m^2	10	Du et al. (2003)

